Biomedical Physics & Engineering Express

PAPER

Fine-tuning the H-scan for discriminating changes in tissue scatterers

RECEIVED
17 February 2020

REVISED
28 April 2020

ACCEPTED FOR PUBLICATION
11 May 2020

PUBLISHED
19 May 2020

Kevin J Parker and Jihye Baek

Department of Electrical & Computer Engineering, University of Rochester, Rochester, New York 14627, United States of America

E-mail: kevin.parker@rochester.edu

Keywords: ultrasound, scattering, tissue characterization, imaging, Rayleigh, pulse-echo

Abstract

The H-scan approach ('H' denoting hue, or Hermite) is a recent *matched filter* methodology that aims to add information to the traditional ultrasound B-scan. The theory is based on the differences in the echoes produced by different classes of reflectors or scatterers. Matched filters can be created for different types of scatterers, whereby the maximum output indicates a match, and color schemes can be used to indicate the class of scatterer responsible for echoes, providing a visual interpretation of the results. However, within the theory of weak scattering from a variety of shapes, small changes in the size of the inhomogeneous objects will create shifts in the scattering transfer function. In this paper, we argue for a *general power law transfer function* as the canonical model for transfer functions from most normal soft vascularized tissues, at least over some bandpass spectrum illuminated by the incident pulse. In cases where scatterer size and distributions change, this produces a corresponding shift in center frequency, along with time and frequency domain characteristics of echoes, and these are captured by matched filters to distinguish and visualize in color the major characteristics of scattering types. With this general approach, the H-scan matched filters can be set to elicit more fine grain shifts in scattering types, commensurate with more subtle changes in tissue morphology. Compensation for frequency-dependent attenuation is helpful for avoiding beam softening effects with increasing depths. Examples from phantoms and normal and pathological tissues are provided to demonstrate that the H-scan analysis and displays are sensitive to scatterer size and morphology, and can be adapted to conventional imaging systems.

1. Introduction

The mathematical treatment of scattering of light and sound has a rich history spanning over 100 years. The scattering of ultrasound from tissues forms the basis for the worldwide use of ultrasound imaging for diagnostic purposes, and an uncountable number of these images are obtained every day. It is generally understood that inhomogeneities within tissues, specifically localized changes in acoustic impedance or density and compressibility, are responsible for the echoes that are captured by imaging systems. A longstanding goal within the research community has been to supplement the traditional B-scan image of tissue with additional quantitative information about the scatterers, linked to the structure or size or statistical properties of the underlying tissue and cellular structures (Lizzi *et al* 1983, Mamou and Oelze 2013). However, recently, a new hypothesis has been formulated that the cylindrical-shaped fluid vessels within tissue parenchyma are predominantly responsible for the echoes commonly captured by imaging systems (Parker *et al* 2019, Parker 2019a, 2019b). Within this framework and within a more general framework encompassing different classical scattering models, the H-scan analysis can be helpful in discriminating between tissue types (Parker 2016a, 2016b, Khairalseed *et al* 2017, Ge *et al* 2018, Khairalseed *et al* 2019a, 2019b). In essence, the H-scan seeks to make a matched filter for the case of a bandpass ultrasound pulse incident on a tissue scatterer or reflector, and producing an echo. The output of a set of matched filters covering the different types of expected scatterers, shown in figure 1, can be examined to determine a best fit to any particular echo or segment, and this additional information can be

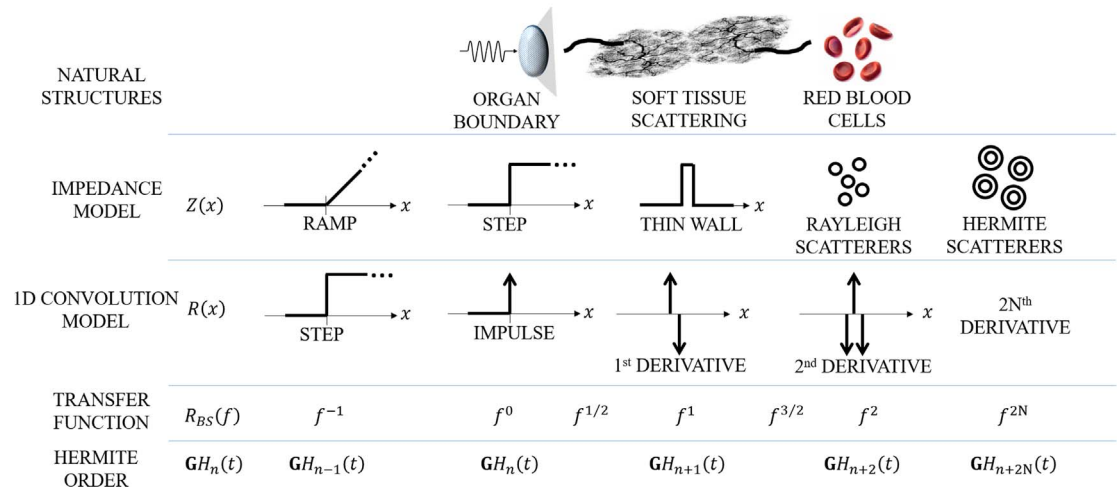

Figure 1. Schematic of shapes of inhomogeneities that cause reflections, with specific transfer functions in the frequency domain, creating specific orders of Gaussian weighted Hermite functions as echoes. Right to left is ordered in increasing power of the frequency domain reflection function. Second row: Acoustic impedance $Z(x)$ shows a ramp function, a step function, a thin wall, Rayleigh scatterers, and Hermite scatterers. Third row: the corresponding reflections under the convolution model, obtained by spatial derivative of the impedance function; a step (corresponding to an integration function), an impulse, a doublet (corresponding to a first derivative), a second derivative, and higher order derivatives. Note that soft tissue scattering sites can correspond to fractional orders above or below unity. Fourth row: frequency domain transfer function corresponding to integration f^{-1}, all pass f^0, derivative f^1, second derivative f^2, and higher order derivatives f^{2N}. Bottom row: Matched filter order from the Gaussian weighted Hermite family corresponding to each structure, assuming a round trip impulse response of the transmitted pulse as a $\mathbf{G}H_n(t)$ function. Most natural structures within tissues are thought to be within the f^0 to f^2 range, thus this range represents the core region for fine tuning of the H-scan analysis.

encoded as a color overlay or a quantitative map. In this way the H-scan analysis provides relatively high resolution and localized information about the nature of the underlying tissue.

In this article we make a series of arguments leading to the fine-tuning of the H-scan analysis for more sensitive discrimination of small changes in scatterers within different regions or over time in response to the progression of disease or the effects of therapy. First, an examination of scattering literature concludes that the transfer function of soft normal vasculature can be approximated as a power law function, at least over some bandwidth of a bandpass interrogating pulse. Secondly, subtle shifts in the size and distribution of scatterers alter the power law and alter the spectrum of the reflected echoes. These expected changes are detected by matched filters in the H-scan process. However, these effects can be skewed by strong frequency-dependent attenuation. After careful compensation for attenuation, the H-scan bank of matched filters is capable of discriminating between the shifts in spectral characteristics.

2. Theory

2.1. The classes of scattering structures

Considering the many different theories of scattering from inhomogeneities, and then all of the different types of scatterers and reflectors within tissues, we seek a coherent framework for characterizing the nature of tissue scattering in order to apply sensitive matched filters to distinguish between the classes. As an overview, it should be noted that the exact solutions for strong scatterers such as spheres and cylinders can be very complex, requiring infinite series of spherical or cylindrical Green's functions (Faran Jr 1951, Born and Wolf 1980). The situation becomes more tractable in the case of weak scattering using the Born approximation (Rayleigh 1918, Morse and Ingard 1987, Insana *et al* 1990, Insana and Brown 1993), where closed form solutions in terms for scattered waves can be formulated as a type of a spatial Fourier transform of the scatterer shape, or else in the case of random structures, as a transform of the correlation function (Debye and Bueche 1949). Another useful simplified framework comes from viewing the pulse echo process as a convolution (Macovski 1983). Within the convolution framework and assuming generic bandpass pulses, it can be shown that the transfer function of structures or scatterers can sometimes be viewed as simple frequency domain functions (power laws in frequency f) corresponding to a perfect plane reflector (all pass filter or transfer function f^0), or a derivative (f^1), or in-between. For example, the ensemble average amplitude from the liver has been estimated as approximately $f^{0.7}$ (Chivers and Hill 1975, Bamber 1979, Campbell and Waag 1984, Parker *et al* 2019, Parker 2019b), consistent with the expected scattering from the fractal branching vasculature. Transfer functions can vary in power law, for example f^2 Rayleigh scatterers such as a red blood cells. In figure 1 in the column under red blood cells is shown its model as simple impedance inhomogeneity, below that its one-dimensional convolution model

(f^2 is the transfer function of a second derivative), its frequency domain representation, and finally the form of the return echo from an incident $\mathbf{G}H_n$ pulse according to a simple convolution model, where $\mathbf{G}H_n$ are Gaussian-weighted Hermite functions, a useful bandpass model. Theoretically, even higher power law transfer functions above f^2 are possible for specially constructed Hermite scatterers (Parker 2017, Astheimer and Parker 2018). Schematically, this framework of scattering from structures and tissues is depicted in figure 1 and some specific details will be explored in the following sections.

2.2. Convolution models

Assume a broadband pulse propagating in the x direction is given by separable functions:

$$P\left(y,\, z,\, t-\frac{x}{c}\right) = G_y(y,\, \sigma_y)G_z(z,\, \sigma_z)P_x\left(t-\frac{x}{c}\right), \tag{1}$$

where $G_y(y,\, \sigma_y) = \exp\left[-y^2/2\sigma_y^2\right]$, i.e., Gaussian in the y and similarly in the z directions, and where the pulse shape P_x in the x direction is given by:

$$\begin{aligned} P_x(x) &= GH_4\left(\frac{x}{\sigma_x}\right)\exp\left(-\frac{x}{\sigma_x}\right)^2 \\ &= 4\mathbf{e}^{-x^2/\sigma_x^2}\left[3-12\left(\frac{x}{\sigma_x}\right)^2+4\left(\frac{x}{\sigma_x}\right)^4\right], \end{aligned} \tag{2}$$

where GH_4 is a fourth-order Hermite polynomial for the pulse shape with a spatial scale factor of σ_x (Poularikas 2010, Parker 2016a), representing a broadband pulse. Its spatial Fourier transform is then:

$$\begin{aligned} {}^{3D}\mathcal{J}\left\{P(x,\, y,\, z)\right\} &= (16\mathbf{e}^{-k_x^2\pi^2\sigma_x^2}k_x^4\pi^{9/2}\sigma_x^5) \\ &\times(\mathbf{e}^{-2k_y^2\pi^2\sigma_y^2}\sqrt{2\pi}\,\sigma_y)(\mathbf{e}^{-2k_z^2\pi^2\sigma_z^2}\sqrt{2\pi}\,\sigma_z), \end{aligned} \tag{3}$$

where we use Bracewell's convention (1965) for the form of the Fourier transform. Using a 3D convolution model (Bamber and Dickinson 1980, Macovski 1983, Prince and Links 2015), we will determine the *dominant* echoes.

In the convolution model, the echo transform is given by the product of the transforms:

$$\begin{aligned} {}^{3D}\mathcal{J}\left\{\text{echo}(x,\, y,\, z)\right\} &= \mathcal{J}^{3D}\left\{p(x,\, y,\, z)\right\}\cdot(k_x)^2\mathcal{J}^{3D} \\ &\times\left\{\text{scatterer}(x,\, y,\, z)\right\} = ((16\mathrm{e}^{-k_x^2\pi^2\sigma_x^2}k_x^4\pi^{9/2}\sigma_x^5) \\ &\times(\mathrm{e}^{-2k_y^2\pi^2\sigma_y^2}\sqrt{2\pi}\,\sigma_y)(\mathrm{e}^{-2k_z^2\pi^2\sigma_z^2}\sqrt{2\pi}\,\sigma_z)) \\ &\cdot(k_x)^2{}^{3D}\mathcal{J}\left\{\text{scatterer}(x,\, y,\, z)\right\}, \end{aligned} \tag{4}$$

where the $(k_x)^2$ term pre-multiplying the cylinder transform stems from the Laplacian spatial derivative in the Born scattering formulation (Rayleigh 1918, Morse and Ingard 1987) and in the 3D convolution model (Gore and Leeman 1977, Bamber and Dickinson 1980). One can consider the last two terms of equation (4) as the frequency domain transfer function which can change the shape of the interrogating pulse. This is examined further in the next section.

2.3. The scattering transfer function

From the earliest tissue characterization work in ultrasound to today, many investigations into soft tissue scattering have reported the frequency dependence of scattering as commensurate with a power law (Chivers and Hill 1975, Gramiak *et al* 1976, Waag *et al* 1976, Chivers 1977, Bamber 1979, Wear *et al* 1995, Nam *et al* 2013, Wei *et al* 2018). This is consistent with some theories of distributions of scatterers over a range of sizes, or a fractal distribution of scatterers, or cylindrically-shaped weak scatterers, or random scatterers with standard correlation functions (Chivers and Hill 1975, Waag *et al* 1976, Bamber 1979, Javanaud 1989, Parker 2019b). Early in the ultrasound tissue characterization era, Bamber (1979) noted the power law behavior seen in measurements from that period. He also pointed out that different theoretical models of Born scattering from both deterministic shapes and random structures, all trended from long wavelength Rayleigh scattering of f^4 (in intensity), but then gradually decreased in power law as frequency increased. The details of this power law trend depend of course on the specific model but the general implication is that over any limited bandwidth, scattering can be approximated as a power law function of frequency.

Thus, our working approximation is that a bandpass interrogating pulse in tissue will be scattered according to a power law transfer function; in terms of echo amplitude this transfer function is likely to vary within a range of approximately f^2 at low frequencies to f^0 at higher frequencies approaching $ka = 1$. This power law transfer function will then shift the peak frequency of the interrogating pulse spectrum, which will be analyzed in the next sections.

2.4. Generalization of backscatter for Hermite transmit functions; non-integer power laws

We assume a broadband transducer is used to produce a pulse with a round-trip impulse response. We consider two bandpass models that are relevant, first the Gaussian-weighted Hermite functions which have precise and useful derivative relations, and then the standard Gaussian spectrum which has been widely used in pulse-echo models since at least the early 1980s (Kuc 1984). First, consider a Gaussian-weighted Hermite function, in this case of order 4, which we designate as $\mathbf{G}H_4(t/\tau)$, where τ is a scale factor:

$$p(t) = 4\mathbf{e}^{-\frac{t^2}{\tau^2}}\left(4\left(\frac{t}{\tau}\right)^4-12\left(\frac{t}{\tau}\right)^2+3\right), \tag{5}$$

and its Fourier transform is:

$$\mathcal{J}\left\{p(t)\right\} = 4\mathbf{e}^{-(f\pi\tau)^2}f^4\pi^{9/2}\tau^5. \tag{6}$$

The spectral peak occurs at $f_{\max}=\sqrt{2}/\pi\tau$. The time and frequency domain representations of this function are shown in figures 2(a) and (b), respectively.

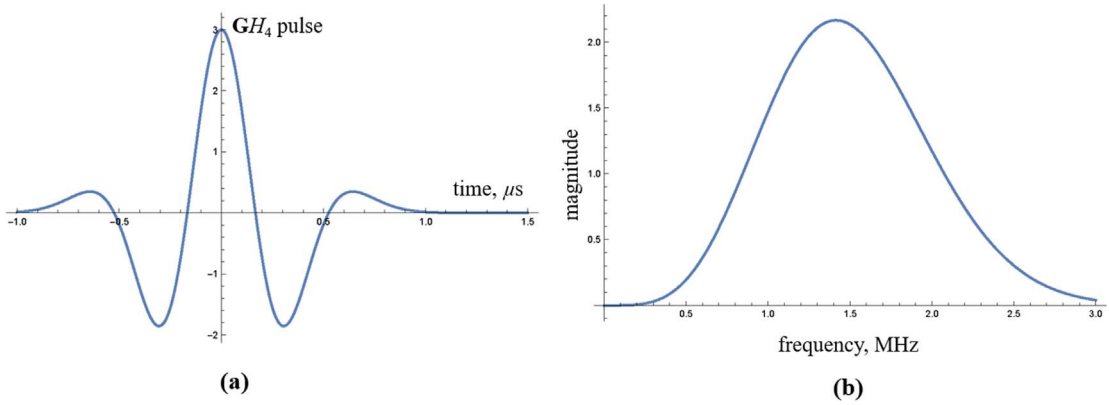

Figure 2. (a) $\mathbf{G}H_4(t/\tau)$ round-trip pulse shape where τ is $1/\pi$ μ s. Its Fourier transform is shown in (b) as a function of f. This time-frequency model is specific to the *GH* family, but is a reasonable representative of a wider class of broadband ultrasound pulses.

Now we assume the convolution model with the transfer function from scatterers of $|f|^\gamma$, where for ensemble averages over liver, we expect γ to be near 0.7 (Campbell and Waag 1984). Note also that our choice of the transfer function as a real and even function of frequency implies that a real and even transmit pulse like the $\mathbf{G}H_4$ will, upon convolution with the scatterer, return an echo that remains real and even in form. In the frequency domain, the transform of the echo is given by the product of the pulse and the transfer function, thus

$$\mathcal{J}\{p(t)\} \cdot |f|^\gamma = 4f^{(4+\gamma)}\mathbf{e}^{-(f\pi\tau)^2}\pi^{9/2}\tau^5 \text{ for } f > 0. \tag{7}$$

The inverse transform of this yields:

$$\mathbf{e}(t) = \frac{4}{\pi^{(\gamma+1/2)}}\left(\frac{1}{\tau}\right)^\gamma \text{Gamma}\left(\frac{5+\gamma}{2}\right) \times \text{Hypergeometric1F1}\left(\frac{5+\gamma}{2}, \frac{1}{2}, -\frac{t^2}{\tau^2}\right), \tag{8}$$

where the hypergeometric function is defined in chapter 15 of Abramowitz and Stegun (1964). This function has the bandpass appearance similar to that shown in figure 4, but with an upshifted frequency content for positive γ.

It can be shown that for the echo spectrum of equation (7), the peak frequency $f_{\max}$ is given by:

$$f_{\max} = \frac{\sqrt{(4+\gamma)}}{\sqrt{2}\pi\tau}. \tag{9}$$

This produces a relatively subtle shift in peak frequencies when tissue structures produce limited variations in γ around 0.7 because the square root of the $4+\gamma$ term in the numerator governs this effect, thus the fine tuning of the H-scan or matched filter operations requires examinations of these incremental shifts.

We note that similar effects are produced when alternative pulses are transmitted. Although the $\mathbf{G}H_n$ pulses have general bandpass properties, some other specific models have been frequently used in simulations. For example, if we use a sine-modulated Gaussian pulse, then:

$$p_g(t) = \exp\left(-\frac{t^2}{2\tau^2}\right)\sin(2\pi f_0 t), \tag{10}$$

and

$$P_g(f) = -i\tau\sqrt{\frac{\pi}{2}}\left[\mathbf{e}^{-2(f-f_0)^2(\pi\tau)^2} - \mathbf{e}^{-2(f+f_0)^2(\pi\tau)^2}\right]. \tag{11}$$

After convolution with the scatterer transfer function of $|f|^\gamma$, the return echo can also be expressed in terms of hypergeometric functions. In the frequency domain, a shift caused by the power law can be calculated. For the Gaussian-shifted spectrum defined above, after multiplication by $|f|^\gamma$ the peak is:

$$f_{\max} = \frac{1}{2}\left(f_0 + \sqrt{\frac{\gamma}{\pi^2\tau^2} + f_0^2}\right). \tag{12}$$

In this case a matched filter can be approximated by shifted Gaussians, and the similarity to $\mathbf{G}H_n$ functions can be quite close. However, the $\mathbf{G}H_n$ family retains the advantage of possessing exact derivative relationships between integer orders (Poularikas 2010).

2.5. Effect of attenuation

For the functions $\mathbf{G}H_n(t)$, derived from the n^{th} derivative of a Gaussian (Poularikas 2010, Parker 2016b), we have the general frequency domain Fourier transform representation

$$\mathcal{J}\left\{\mathbf{G}H_n\left(\frac{t}{\tau}\right)\right\} = \frac{f^n\tau^{n+1}\mathbf{e}^{-(f\pi\tau)^2}}{\sqrt{2}} \tag{13}$$

for integers $n > 0$ and $f > 0$.

The peak frequency $f_{\max}$ is determined by taking the first derivative with respect to f and finding its zero. The result is $f_{\max} = \sqrt{n/2}/\pi\tau$ for the $\mathbf{G}H_n(t/\tau)$ family. If one of this class of pulses is used in tissue backscatter imaging with a tissue comprised of scatterers with an ensemble average spectral magnitude of $|f^\gamma|$ and an attenuation of $\mathbf{e}^{-\alpha \cdot f \cdot x}$, then the transfer

function will be in the frequency domain:

$$\mathcal{J}\{p(t)\} = 4f^{(4+\gamma)}\mathbf{e}^{-(f\pi\tau)^2}\pi^{9/2}\tau^5\mathbf{e}^{-\alpha\cdot f\cdot x} \text{ for } f > 0. \tag{14}$$

The peak frequency will be influenced by their product. Again, using the first derivative to find the peak frequency of the altered spectrum results in:

$$f_{\max}(\gamma, \alpha, x, \tau, n) = \frac{\sqrt{8(n+\gamma)\pi^2\tau^2 + \alpha^2x^2} - \alpha x}{4\pi^2\tau^2} \tag{15}$$

for $\{\gamma, \alpha, x, \tau, n\} > 0$. As $\gamma \to 0$ and $\alpha x \to 0$, the result approaches the original spectral peak of the Hermite function, $f_{\max} = \sqrt{n/2}/\pi\tau$. As will be shown in the Results section, the strong cumulative effects of attenuation can mask any subtle change in scattering power law behaviors due to alterations of tissue structure.

Alternatively, if a conventional bandpass Gaussian pulse is utilized, a corresponding frequency can be calculated. For the expected spectral magnitude of the returned echo modeled as

$$P_g(f) = (A_0\mathbf{e}^{-(f-f_0)^2/2\sigma_f^2})|f^\gamma|(\mathbf{e}^{-\alpha\cdot f\cdot x}) \text{ where } f > 0, \tag{16}$$

the peak frequency is given by

$$f_{\max}(f_0, \sigma_f, \gamma, \alpha, x) = \frac{1}{2}(f_0 - \alpha\sigma_f^2 x + \sqrt{4\gamma\sigma_f^2 + (f_0 - \alpha\sigma_f^2 x)^2}). \tag{17}$$

These functions display a nearly linear downshift in peak frequency with depth for typical parameters found in human abdominal ultrasound. In equation (17) f_0 is determined by the round-trip impulse response and results from the scatterers within tissue. In some cases, there is no reference impulse response available and average spectra are sampled from a region of interest within tissue, and then curve-fit to a Gaussian spectrum. In that case, we can re-interpret equation (17) with $f_{\max}$ as the observed ensemble average peak and γ implicitly as 0, thus the equation reduces to

$$f_{\max}(f_0, \sigma, x) = f_0 - \alpha\sigma_f^2 x, \tag{18}$$

or as an estimate from plotting the data:

$$\hat{\alpha} = \left(\frac{\Delta f_{\max}}{\Delta x}\right)\cdot\left(-\frac{1}{\sigma_f^2}\right) \tag{19}$$

using the slope of $f_{\max}$ versus depth. A linear downshift was first derived for attenuating media and a Gaussian pulse by Kuc (1984). For completeness, we note there are many additional estimators for attenuation that have been proposed over the last four decades (Cloostermans and Thijssen 1983, Parker and Waag 1983, Parker 1983, Maklad *et al* 1984, Parker *et al* 1984, Parker and Tuthill 1986, Garra *et al* 1987, Parker *et al* 1988, Zagzebski *et al* 1993, Fujii *et al* 2002, Lee *et al* 2012, Tai *et al* 2019). More comprehensive analyses include the effects of beam diffraction and other system parameters (Mamou and Oelze 2013).

2.6. Compensation for attenuation

Here we proposed an inverse filter approach to the compensation of attenuation. Once estimated by the downshift formulas, the inverse filter in the frequency domain is approximated as a real and even exponential increase as a function of frequency and depth. In practice, some upper band limit must be imposed to ensure finite energy and avoid unproductive amplification of noise. In the continuous domain, we note that a practical, finite energy inverse filter

$$\text{Infil}(\alpha, x, f, \sigma_f) = \exp(+\alpha x f)\exp\left(-\frac{f^2}{2\sigma_f^2}\right) \text{ for } f > 0 \tag{20}$$

will have positive amplification out to some frequency set by the σ_f parameter, taken to be consistent with the transmit pulse's upper frequency range. If implemented as a time domain convolution, assumed to be a real and even function of time and frequency, the impulse response of this can be expressed in terms of Gaussian and erf functions, in which the complex terms appear as conjugates so the overall result is also real and even. In digital signal processing, this can be implemented as an IIR or an FIR discrete time filter of the sampled echoes.

Of course this inverse filter is depth-dependent, however the convolution for any increment of x can be repeated over subsequent increments of $2x$, $3x$, $4x$, and onward since repeated convolutions in the time domain are equivalent to multiplications in the frequency domain, and $\exp(f\cdot\alpha\cdot x)^N = \exp(f\cdot\alpha\cdot N\cdot x)$ for real and positive values of the arguments.

3. Methods

3.1. Attenuation correction

The ultrasound signal is emitted from a transducer as shown in figure 3, and we assume the RF echoes from tissue scatterers in the absence of attenuation would be RF(x), where x is the propagated distance from the probe.

Due to the attenuation the received ultrasound intensity can be described as $\text{RF}(x)\cdot e^{-\alpha f x}$ where α is the attenuation coefficient in NP/cm/MHz and f is frequency of ultrasound in MHz. The received ultrasound is compensated depending on depth in the time gain compensation (TGC) amplifier, which is a practical component of ultrasound systems. To reconstruct the transmitted signal when the gain function is not recorded, we assume that the TGC was set properly to a function of depth so as to approximately compensate for attenuation, proportional to $e^{+\hat{\alpha}_0 x}$ at the depth x and $\hat{\alpha}_0$ is an *a priori* estimate of attenuation in

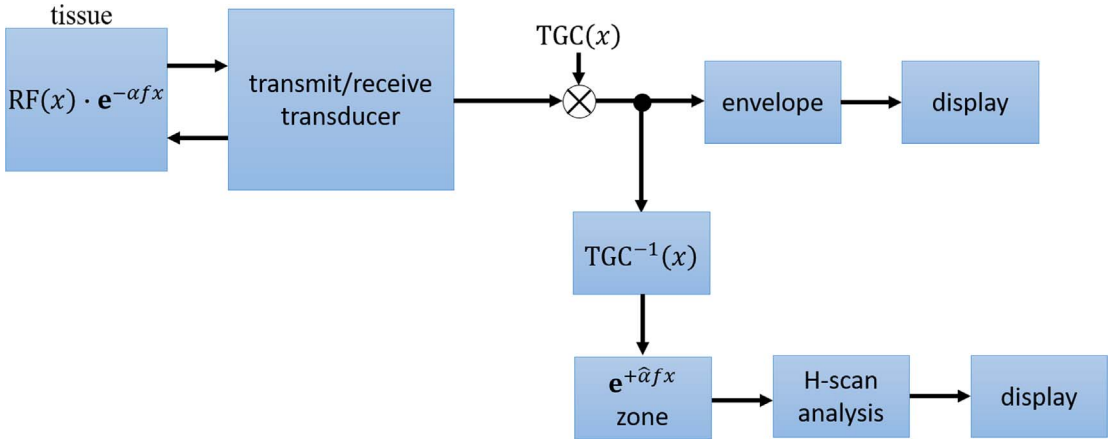

Figure 3. Schematic for attenuation correction.

Np/cm. Therefore, the unamplified ultrasound signal is reconstructed as

$$\mathrm{RS}(x) = \mathrm{RF}(x) \cdot \mathrm{TGC}^{-1}(x). \tag{21}$$

To compensate for frequency-dependent attenuation, the transmitted signal can be reconstructed in frequency domain at some selected depth:

$$\mathcal{J}\{\mathrm{RS}(x)\} \cdot \mathcal{H}(f), \tag{22}$$

where $\mathcal{H}(f)$ is a frequency domain function to compensate for frequency-dependent attenuation. In this study, we assume $\mathcal{H}(f)$ is proportional to $e^{+\alpha_0 fx}$ within a defined region of interest (ROI) and spectral bandwidth. This is a depth-dependent filter, however to simplify the implementation, we define several zones in the depth direction. Each zone has one nominal depth, x_z for each zone z. The reconstructed transmitted signal results in:

$$\mathcal{J}\{\mathrm{RS}(x)\} \cdot \mathcal{H}_z(f) = \mathcal{J}\{\mathrm{RS}(x)\} \cdot e^{\alpha f x_z} \tag{23}$$

for $z = \{1, 2, \ldots, n\}$, where n is the number of zones. The limited dynamic range of receiver amplifiers and noise floor will always present a limit as to how far in depth the correction can be taken. Similarly, the practical upper limit of the pulse bandwidth in equation (23) may require an upper limit to the inverse filter as given in equation (20).

3.2. Estimation of attenuation coefficient

For the attenuation correction in section 3.1, we used one estimated attenuation coefficient for the same target when we perform multiple scans. To estimate the attenuation coefficient, the frequency spectrum can be modeled using Gaussian pulse and attenuation of ultrasound, in accord with equations (17)–(19). To simply compensate for the depth-dependent variables in the frequency domain spectra, we partitioned the ultrasound signal into several depth regions, for example it can be five zones along the axial direction, as shown in figure 4, or more zones for longer (deeper) ROIs.

The estimate of the attenuation coefficient within the ROI is derived from the slope of $f_{\max}$ versus depth. The peak frequency for each zone is estimated from a Gaussian fit of the ensemble average spectrum, which is the Fourier transform of ultrasound signal in time domain from each zone, averaged across the ROI scan lines at constant depth. By selecting the maximum value of the smoothed frequency spectrum, the peak frequency for each zone can be estimated as a function of depth, and subsequently a linear fit of peak frequency versus depth is calculated according to equations (18) and (19) to yield a single attenuation estimate over the ROI; this approach is shown in figure 5. The zones in this study were each several mm in depth, depending on frequency and bandwidth of different scans, and sufficient to establish reasonable resolution in both time and frequency.

3.3. H-scan convolution

The H-scan concept is based on convolution with *matched filters* corresponding to specific sized scatterers. In figure 6, five different matched filters with different peak frequency were used to obtain convolution images of a phantom, using a 6.4 MHz center frequency transducer. The filters with the smallest peak frequency in figure 6(b) highlighted the target strings in the phantom, corresponding to larger structures; otherwise, figure 6(f) enhanced smaller sized speckles.

In ultrasound images, scatterers from small to large can correspond to smaller speckles to larger structures in the human body. When using different filters, various sized structures in the human body can be matched to specific filters. In this study, Gaussian bandpass functions with 256 peak frequencies were used to obtain convolution between the Gaussian functions and ultrasound echoes RF(x). These correspond to equations (10)–(12), where f_0 is taken as 4.7 MHz and $f_{\max}$ ranges from 1.4 to 7.9 MHz for the case shown in figure 6. The frequencies f_0 and $f_{\max}$ are set depending on the spectrum of the input signal.

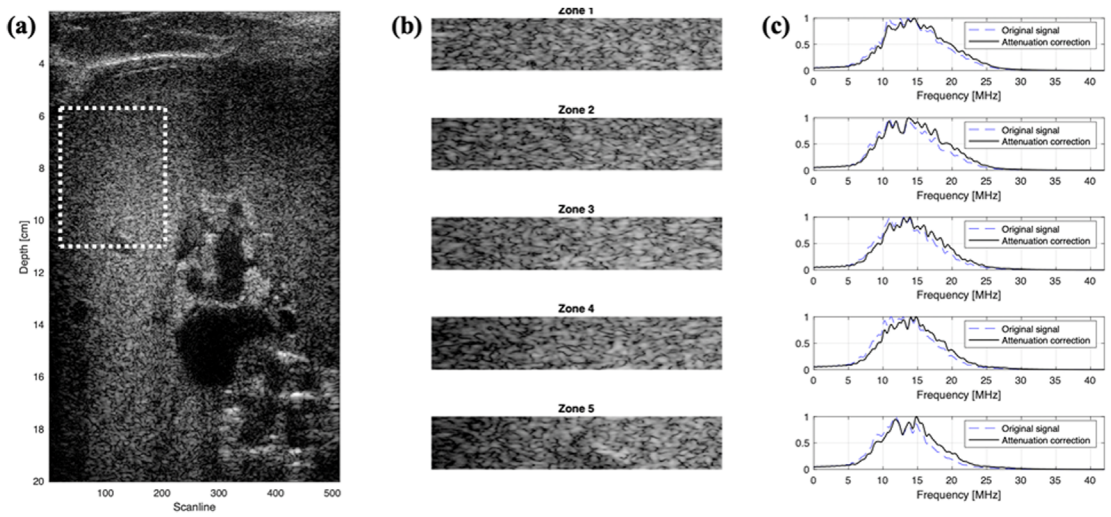

Figure 4. Attenuation-corrected spectra. Five zones.

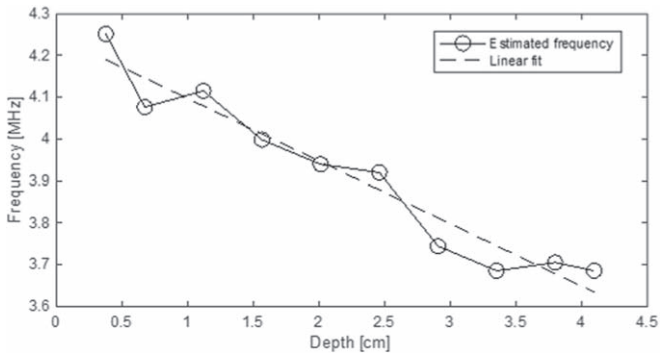

Figure 5. Estimated peak frequencies corresponding to each of 10 zones. The linear fit of this curve is obtained, which can be used to calculate the estimated attenuation coefficient for the tissue within the ROI.

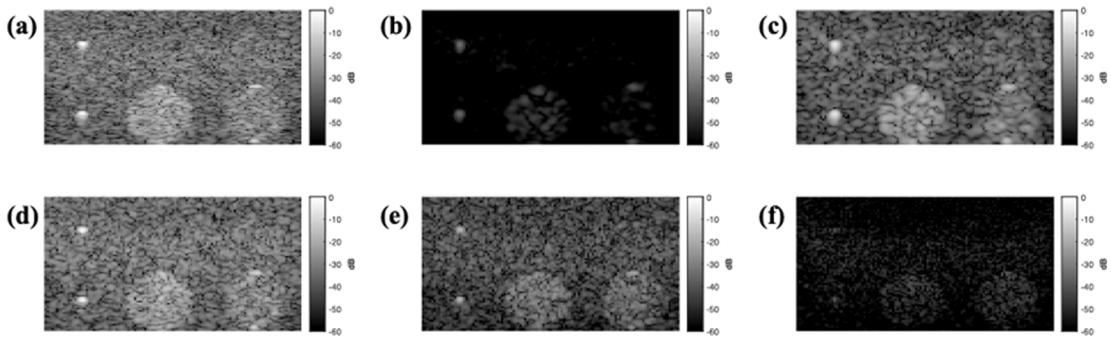

Figure 6. (a) Input ultrasound image. (b)–(f) are convolution images with five different matched filters, whose peak frequencies are 1.4, 3.1, 4.7, 6.3, and 7.9 MHz. The smallest peak frequency filter in (b) highlights the largest structures in the phantom. The largest frequency filter of (f) tends to enhance the smallest speckle structure in the ultrasound image.

Thus, each pixel in the ultrasound image has a corresponding set of 256 convolution values, as shown in figure 7, from which we select a maximum according to the concept of a matched filter. In our experience, these 256 outputs for each pixel have a single maximum; in other words, multiple peaks are unlikely to be observed from soft tissue echoes.

After attenuation correction, the convolution with Gaussian functions is examined to generate H images, which are specific frequency range enhanced signals; in H1, the lowest frequency range signal is amplified, and the highest frequency is enhanced in H256. The selected indices for each pixel correspond to a color map ranging from 1 to 256 RGB colors. Using

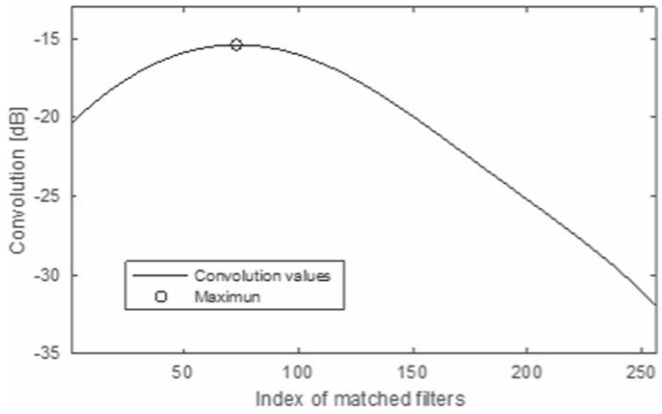

Figure 7. Convolution values for a pixel in ultrasound image. 256 filters were used to get convolution images.

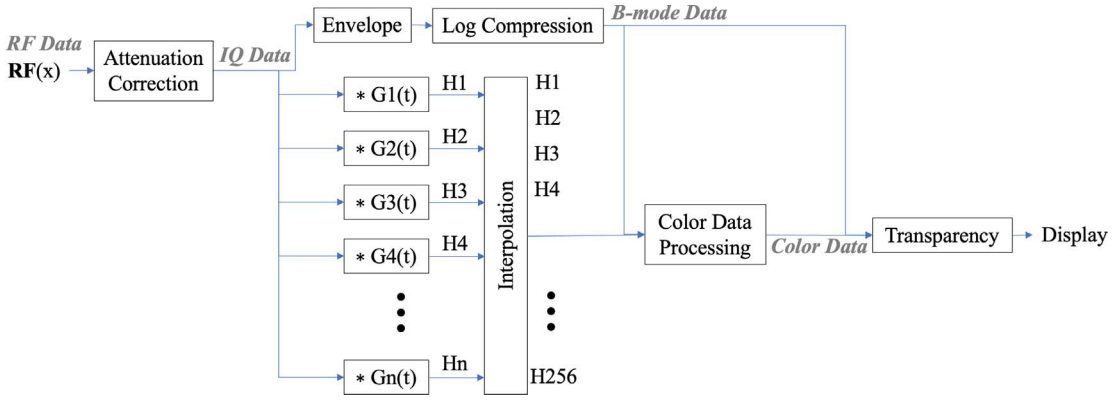

Figure 8. Schematic for H-scan.

transparency overlays to combine the color and B-mode data, the final H-scan image can be displayed, as described in the next section.

3.4. Color map for H-scan

To enhance visualization, a color map for H-scan is proposed, corresponding to the maximum output selected from the matched filter bank. This color map can also be thought of as a way to show the instantaneous frequency of each pixel in an ultrasound image.

A flow chart of H-scan is shown in figure 8. Attenuation-corrected convolution images are assigned as input data for color map processing, which generates the H-scan color map. By combining traditional B-scan and H-scan color map data, a transparency of the two displays the H-scan image; the B-mode contains the highest spatial resolution, and the color map corresponds to peak frequency components.

A color map of 256 levels is set for H scan; the levels 1 to 256 correspond to red to blue colors, sequentially, as shown in figure 9. After the convolution process described in section 3.3, each pixel has one maximum matched filter output determining a specific color map level among 256, as described in figure 9.

3.5. Experimental setup

H-scans with attenuation correction were obtained from *in vitro* and *in vivo* studies. To evaluate the performance of the proposed attenuation correction method, a tissue-mimicking phantom (CIRS 040GSE, Computerized Imaging Reference Systems, Norfolk, VA, USA) was used. This phantom has two zones with higher and lower attenuation, whose attenuation coefficients were 0.5 and 0.7 dB/cm/MHz. For this phantom study, a Verasonics ultrasound scanner (Verasonics, Kirkland, WA, USA) with a linear array transducer (L7-4, ATL, Bothell, WA, USA) acquired RF signal at the center frequency of 5 MHz and 6.4 MHz for plane wave and focused wave, respectively. Coherent plane wave compounding (Montaldo *et al* 2009) was implemented to obtain beamformed RF data. TGC data were not recorded for all the scans and so were assumed to have been increasing exponentially with depth as described in section 3.1.

For *in vivo studies*, rat and mouse liver data were used and there are three kinds of data: normal, hepatic fibrosis, and cancerous. For the hepatic fibrosis data, a Vevo 2100 (VisualSonics, Toronto, Canada) with a 21 MHz center frequency linear transducer (MS 250) was used to scan one normal and three fibrotic rats. Separately, a spontaneous murine model for

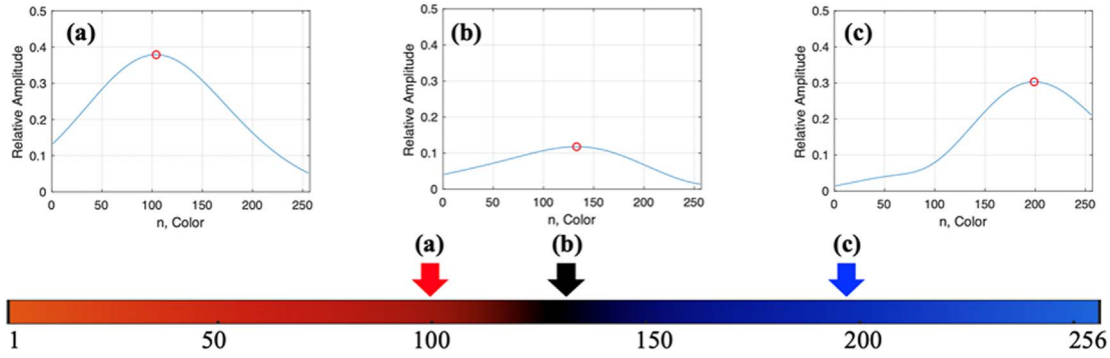

Figure 9. For each pixel in B-mode image, there are 256 matched filter convolution values. By selecting the maximum value, we can generate a color map. (a), (b), and (c) are three pixels in a B-mode image. The *x*-axis represents indices among 256 Gaussian, and the *y*-axis represents relative amplitude of each convolution value. According to maximum amplitudes, (a), (b), and (c) pixels are assigned as red, black, and blue in the RGB color map, respectively.

cholangiocarcinoma (Han *et al* 2019) was imaged using the Vevo 3100 (VisualSonics, Toronto, CA) with a 32 MHz center frequency linear probe (MX 550D). Finally, using a liver metastasis model (Soares *et al* 2014, Ahmed *et al* 2020); a normal and a cancerous mouse were scanned, and a Verasonics (Vantage-256, Verasonics, Kirkland, WA, USA) was used with a L11-5v probe at 10 MHz center frequency. The VisualSonics scanner used focused beam transmission and the Verasonics used plane wave transmission. All *in vivo* animal studies were reviewed and approved by the University Committee on Animal Resources at the University of Rochester or the sponsoring institution.

3.6. Evaluation for H-scan

To evaluate the performance of H-scan, intensity-weighted percentage of blue (IWP_{blue}) and red (IWP_{red}) were defined as follows:

$$(\mathrm{IWP}_{\mathrm{blue}}) = \frac{\sum_{i\in B} I_i}{\sum_{i\in B} I_i + \sum_{i\in R} I_i} \times 100\%$$
$$(\mathrm{IWP}_{\mathrm{red}}) = \frac{\sum_{i\in R} I_i}{\sum_{i\in B} I_i + \sum_{i\in R} I_i} \times 100\%, \qquad (24)$$

where i is index of each pixel in B-mode image and I_i is normalized color intensity for i. The indices, $i \in B$ and $i \in R$, are pixels within the ROI classified as blue and red, respectively.

Our color map in figure 9 ranges from 1 to 256; the lower range of 1 to 128 represents red (reflected echoes have a lower peak frequency), and the upper range of 129 to 256 represents blue (higher peak frequencies). The extreme color map indices of 1 or 256 are displayed as saturated red (lowest frequency matched filter) or blue (highest frequency), respectively, and so red and blue shifts can be quantified by their difference from the middle, denoted as $I_{i\in R}$ and $I_{i\in B}$, respectively. To normalize the color data ranging from 1 to 256, the red colors from 128 to 1 are re-assigned to 0 to 1 in sequence, and the blue colors from 129 to 256 are set to 0 to 1, which is given by:

$$I_{i\in B} = \frac{C_i - 129}{127}, \qquad (25)$$

where C_i is the color map for the ith pixel for blue data, and

$$I_{i\in R} = \frac{128 - C_i}{127} \qquad (26)$$

for red data.

4. Results

4.1. Phantom study

In the phantom study, the attenuation correction method was evaluated using estimated peak frequency and H-scan results. Traditional B-mode image and B-mode after attenuation correction for the phantom are seen in figures 10(a) and (b), respectively. Their peak frequencies were estimated for ten depth zones in figure 10(d). B-mode image has frequency down shift along depth; otherwise, the down shift after attenuation correction is compensated for, resulting in a more flat linear fit of estimated frequency. Figures 10(e) and (f) show H-scan color maps without and with attenuation correction, respectively. More red pixels at increasing depth are observed when attenuation correction is not used for H-scan in figure 10(e). After using the attenuation correction method, red and blue pixels are more uniformly distributed over the entire depth, as shown in figure 10(f). The intensity-weighted percentage of blue and red were averaged for depths and it is presented as a function of depth; figures 10(g) and (h) represent the percentages for the method without and with attenuation correction, respectively. In figure 10(g), red pixel percentage gradually increases, and blue pixels decrease due to the frequency down shift. However, in figure 10(h), the percentage of blue and red pixels are similar with depth, meaning that the frequency attenuation effect is compensated by using the proposed attenuation correction method. As a result, figure 10(c) demonstrates regularly-distributed red and blue colors regardless of depth in the Hscan image.

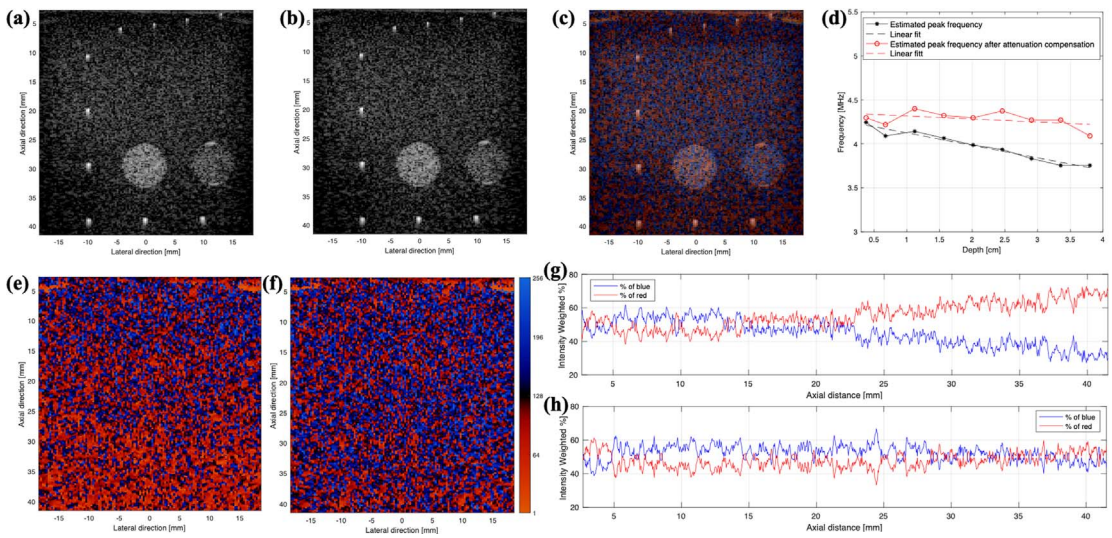

Figure 10. H-scan correction for phantom: nominally 0.7 dB/MHz/cm attenuation. Verasonics L7-4, 5 MHz plane wave transmission frequency. (a) Traditional B-mode, (b) B-mode after attenuation correction, (c) H-scan, (d) Estimated center frequency along imaging depth and curve-fit. (e) H-scan color map for traditional RF signal, (f) H-scan color map for attenuation corrected RF data, (g) Intensity-weighted percentage of blue and red without attenuation correction, and (h) Intensity-weighted percentage of blue and red with attenuation correction.

Other H-scan results for the phantom are shown in figure 11, scanned using focused beam transmission with 6.4 MHz center frequency. The regularly spaced, more echogenic wire targets in the phantom appear more red in color than the background speckle since the size of the wire targets is larger than the background scatterers. To show the H-scan results more clearly, figure 11(d) used threshold in color map, which shows red colored pixels with color map values ranging from 1 to 55. The clustered red colors are positioned at wire targets in the phantom.

4.2. Attenuation correction: *in vivo* study

An *in vivo* scan of a rat liver with grade 4 hepatic fibrosis demonstrates color difference between H-scan images without attenuation correction and with attenuation correction in figure 12. Figure 12(b) shows the frequency down shift: more blue pixels in near depth, and more red pixels in the more distal region. However, after correction the H-scan color distribution in figure 12(c) is not dependent on depth, demonstrating that attenuation is compensated properly, which is consistent with phantom results. The % of blue and red profile along depth in figure 12(d) is altered due to the attenuation effect; on the other hand, after the attenuation correction, the blue and red percentage distribution becomes more uniform as shown in figure 12(e).

The attenuation correction method allows us to correct for color change caused by the frequency down shift; therefore, a color difference is likely to come from variation of tissue characteristics.

In figure 13(b), a spontaneous murine tumor is poorly differentiated from normal tissue because of the shift to more red colors at depth caused by attenuation. After applying the attenuation correction shown in figure 13(c), tumor cells appear more red than normal tissues at the same axial depth.

4.3. H-scan: *in vivo* study

Murine and rat *in vivo* studies with diffuse pathologies demonstrate H-scan visualizations within normal, hepatic fibrosis, and cancerous tissues. To compare hepatic fibrosis and normal liver, the H-scan ROI was set at the same depths in figure 14. For the case of early and late stage tumor, livers were contoured as shown in figure 15. To compare the color and percentage, the H-scan process used the same Gaussian function set for convolution in the figure 14 case; the figure 15 case also used the same Gaussian set. Figures 14 and 15 show obvious color difference between the cases; H-scan results with hepatic fibrosis and severe stage of tumor contain more blue than the other tissues. The hepatic fibrosis case has 61.5% of the intensity-weighted blue percentage, which represents a shift to the smaller scatterers; on the other hand, the normal rat liver has 51.9%. According to figures 14(c) and (f), the hepatic fibrosis case represents a greater difference of distribution between the red and blue pixels in H-scan. For the normalized intensity, the mean value differences between red and blue are 0.18 and 0.03 for hepatic fibrosis and normal tissue, respectively. The p-value between the red and blue scatterer groups for hepatic fibrosis is 1.05×10^{-10}, which is smaller than the p-value of 0.19 for normal, indicating that hepatic fibrosis has more significant difference between the red and blue groups than the normal case; there are no significant differences for normal. In figures 14 and 15, the following notations are used for the statistics: ns (no significance) $p > 0.05$; * $p < 0.05$; ** $p < 0.01$;

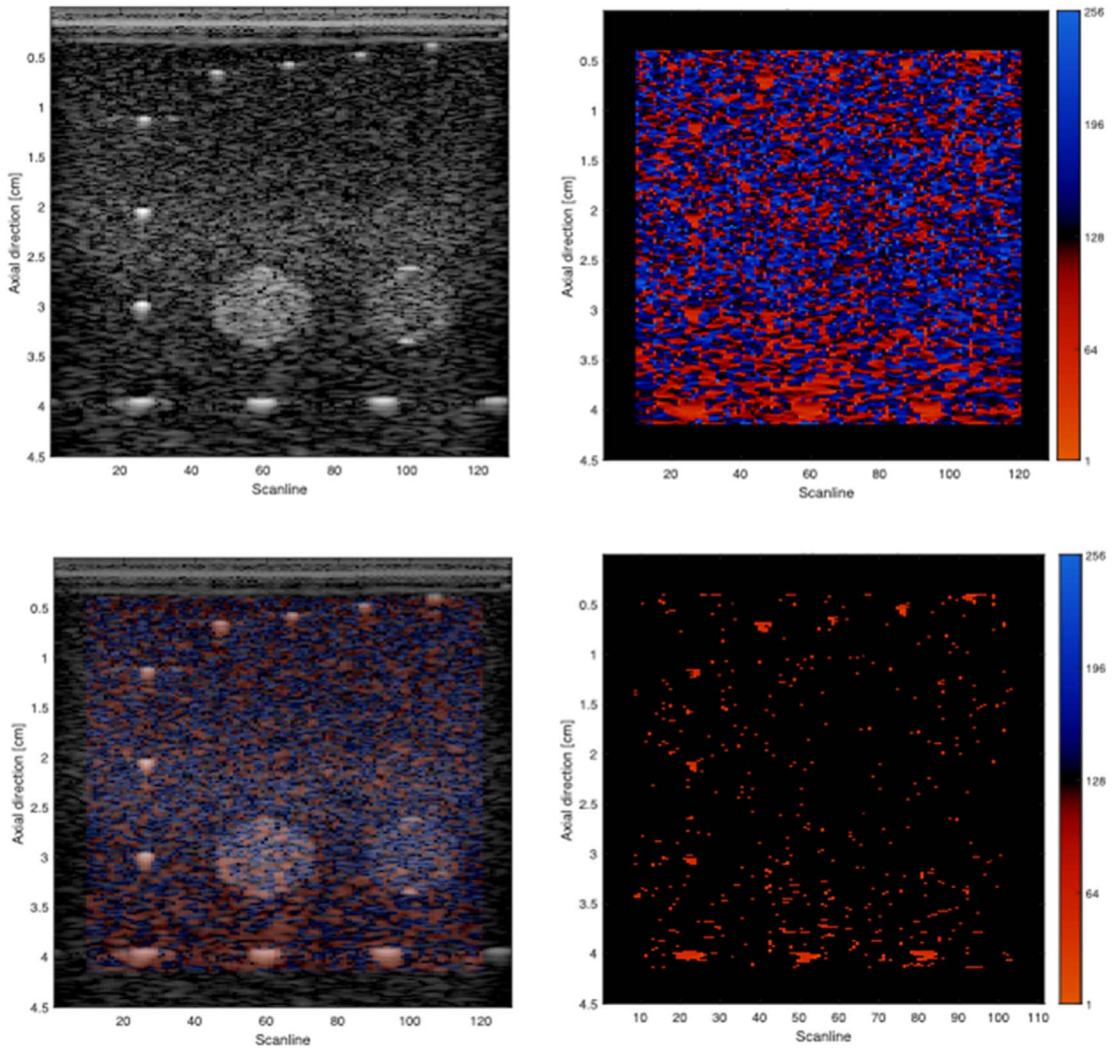

Figure 11. B-scan and H-scan of phantom, 6.4 MHz focused transmit. (a) B-scan, (b) H-scan color map, (c) H-scan image. (d) H-scan color map with threshold to show red pixels ranging from 1 to 55 color map levels, which correspond to relatively larger scatterers in B scan.

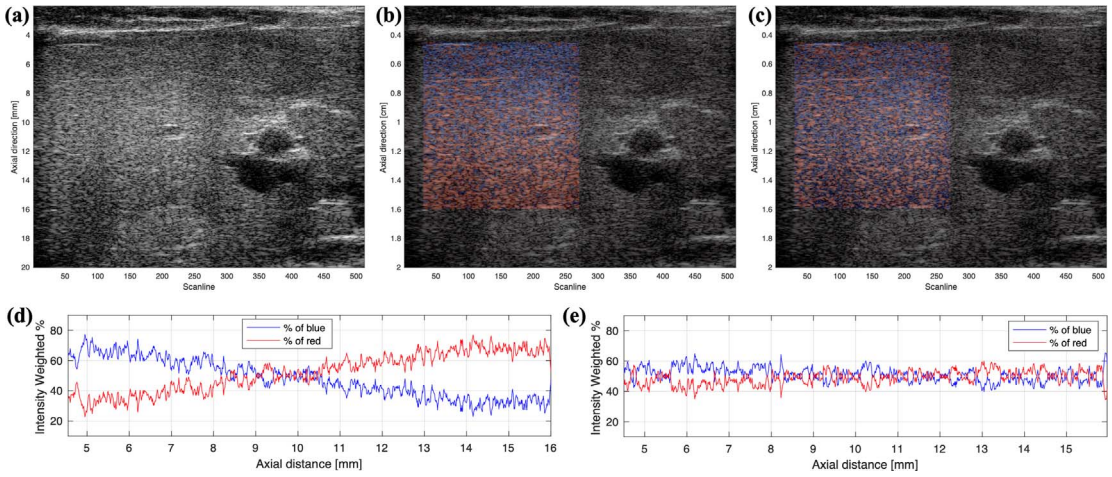

Figure 12. Rat liver data. (a) B-mode, (b) H-scan without attenuation correction, (c) H-scan after attenuation correction, (d) intensity-weighted percentage of blue and red without attenuation correction, and (e) intensity-weighted percentages with attenuation correction.

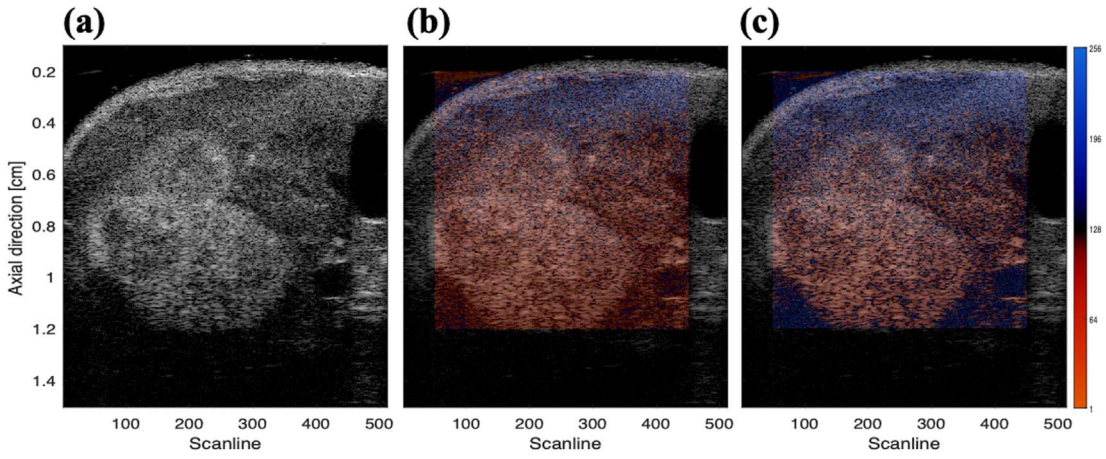

Figure 13. Murine tumor in liver. (a) B-mode, (b) H-scan without attenuation correction, and (c) H-scan after attenuation correction.

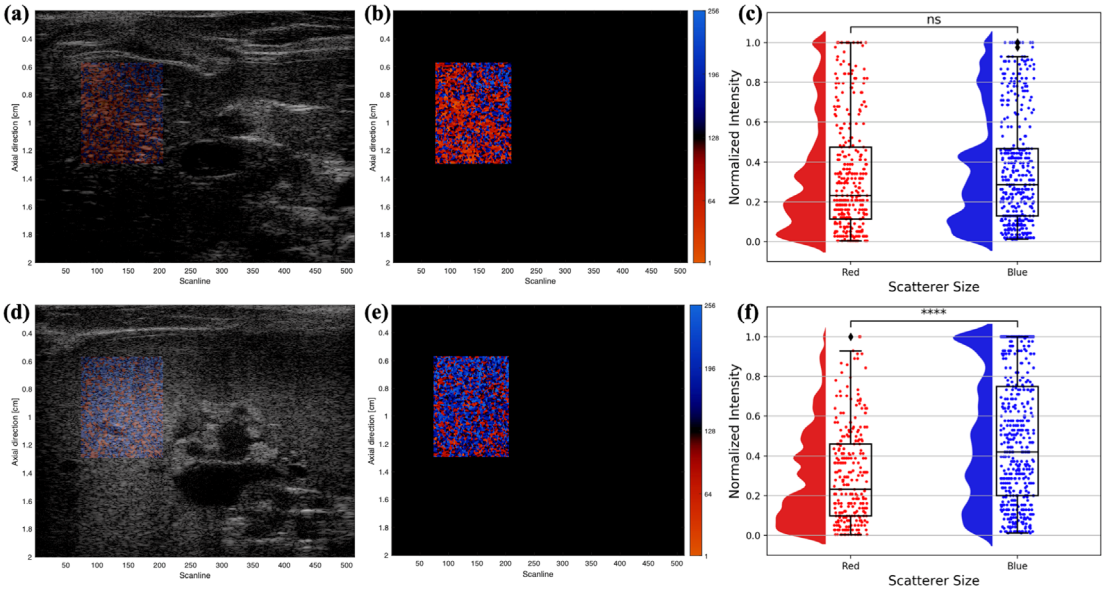

Figure 14. H-scan of normal and abnormal rat livers. The upper row and lower row data are the results of normal and hepatic fibrosis rat, respectively. (a) and (d) show H-scan images with H-scan box, and (b) and (e) show H-scan color map data. (c) and (f) show half violin and half box plots.

*** $p < 0.001$; and **** $p < 0.0001$. In the tumor case, the smaller scatterer percentages are 50.5% for early stage (the first B-scan at 11 days after the injection of cancer cells) and 65.8% for late stage (the last scan at 28 days), and the mean value differences between red and blue are 0.01 for early stage and 0.17 for late stage. For the blue and red distribution in figures 15(c) and (f), late stage metastatic pancreatic ductal adenocarcinoma (PDAC) tumor demonstrates a greater difference compared to early stage PDAC; p-values between red and blue groups are 0.0813 and 1.0597×10^{-10} for early and late stage, respectively.

5. Discussion

Our analysis of transfer functions from different classes of scatterers has led to a generalization in terms of a simple power law function of frequency, whereby shifts in the scattering size or type lead to shifts in the power law. Integer orders of power law 0, 1, and 2, correspond to an all-pass filter, a derivative, and a second derivative, respectively, and structures with these behaviors are easily constructed in the laboratory and may be approximated in tissues under certain conditions (Parker 2016a). Fractional power laws above and below 1 may correspond to a physiological range of fluid-filled vessels modeled as cylinders (Parker 2019b). While the exact solution for specific scatterer shapes can be complicated, the narrowband slope for $ka < 1$ is more easily characterized by power law behavior. This is consistent with a first order expansion, or Taylor's series expansion in log-log space around some frequency. In the long wavelength (Rayleigh scattering) regime the power law is 2,

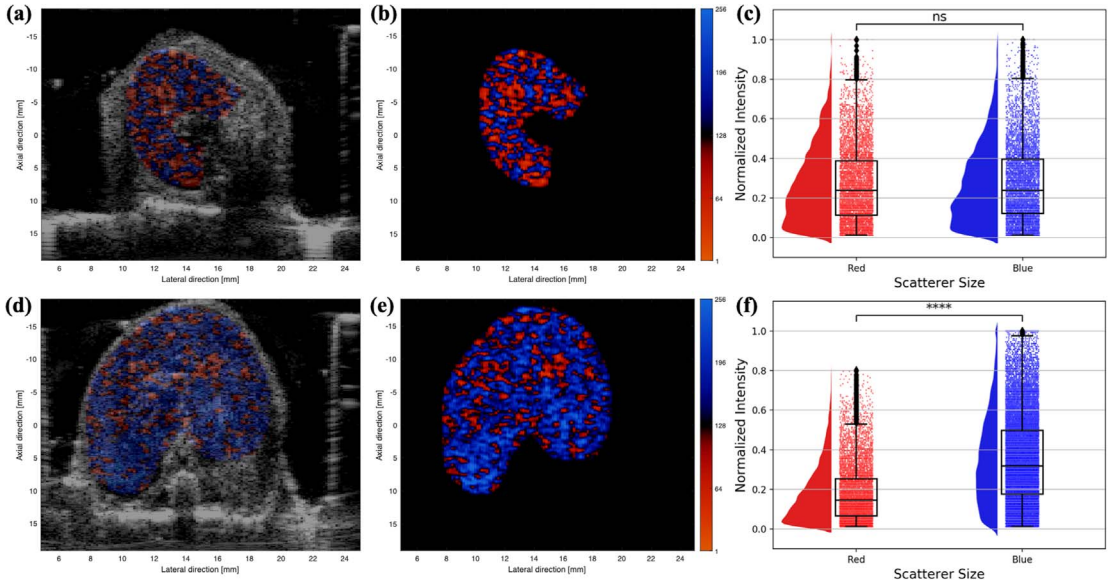

Figure 15. H-scan of early stage and advanced metastatic cancer murine livers. Upper row data are from early stage following injection of cancer cells, and lower row data are from the liver with metastatic cancer at end stage. (a) and (d) are H-scan images. (b) and (e) are H-scan color maps. (c) and (f) show half violin and half box plots. End stage tumor tissues appear significantly more blue.

frequency squared for the amplitude of the scattered wave. As ka increases towards unity the slope decreases, ultimately towards zero as shown by Bamber (1979). The H-scan matched filters can be arranged so as to detect some shifts in the transfer function. We note that historically, bandpass filter banks have been used in ultrasound as frequency diversity approaches to flaw detection (Bilgutay *et al* 1979, Bilgutay and Saniie 1984) and for speckle reduction (Galloway *et al* 1988). The H-scan differs from these in its framework of selecting the matched filter for echoes produced by subtle changes in scattering characteristics.

A practical question involves the minimum sensitivity of the matched filters to subtle shifts in tissue structures. The shift in peak frequency as a function of power law γ and other factors is given by equations (9) and (12) for the case of a $\mathbf{G}H_4$ pulse and a Gaussian pulse, respectively. Also, the functional dependence of the power law a on the cylinder radius is maximum in the long wavelength limit where transfer functions are proportional to frequency squared. Using the chain rule of calculus, for a bandpass pulse with peak spectrum at $f_{\max}$, we can write:

$$\frac{\partial f_{\max}}{\partial a} = \frac{\partial f_{\max}}{\partial \gamma}\left(\frac{\partial \gamma}{\partial a}\right). \tag{27}$$

The first term on the right can be simply obtained for our specific cases by differentiation of either equations (9) or (12) for $\mathbf{G}H_4$ or Gaussian bandpass models, respectively. For example, from equation (9) we have:

$$\frac{\partial f_{\max}}{\partial \gamma} = \frac{1}{2\sqrt{2}\,\pi\tau\sqrt{4+\gamma}}. \tag{28}$$

The second term $(\partial\gamma/\partial a)$ is more complicated since γ is a power law fit, but the derivative with respect to a is linear. However, from the literature (Bamber 1979, Parker 2019b) we observe that the slope in log-log space is 2 at low ka and then slowly decreases to 0 near $ka = 1$ for a number of models. In the important subresolvable zone near $ka = 0.1$ or 0.2, we find generally that $\partial\gamma/\partial a$ is in the range of $k/4$ (units of 1/length). Using this, we have:

$$\frac{\partial f_{\max}}{\partial a} \cong \frac{k}{8\sqrt{2}\,\pi\tau\sqrt{4+\gamma}} \text{ for } 0.1 < ka < 0.2. \tag{29}$$

Now examining the case where the peak frequency was 6 MHz $\cong\sqrt{2}/\pi\tau$, and γ near 2, we have:

$$\begin{aligned}\frac{\partial f}{\partial a} &\cong \left(\frac{k}{16}\right)(6)\left(\frac{1}{\sqrt{4+2}}\right)\\ &\cong\left(\frac{2\pi 6\times 10^{6}\text{rad s}^{-1}}{1.5\times 10^{9}\mu\text{m s}^{-1}}\right)(6\text{MHz})\left(\frac{1}{\sqrt{6}}\right)\\ &\cong 0.01\text{MHz }\mu\text{m}^{-1}\end{aligned} \tag{30}$$

This result is consistent with the findings published previously (Khairalseed *et al* 2017), where changes in scatterer radius on the order of 10 μm were separated by a set of 4 H-scan filters, implying a 0.1 MHz discrimination in outputs.

Limitations of this study include the effect of noise on the performance of the matched filters. As can be inferred from figures 7–9, there can be substantial overlap in the spectra of neighboring matched filters, however from equation (15)–(17), we wish to have fine grain sensitivity to changes in the scattering transfer function. Broadband noise can degrade the correct

choices of a matched filter bank by adding uncorrelated and random components to the signal. These interactions and their parameterization are left for future study, however it can be concluded generally that the accuracy of selecting the correct matching filter will degrade as the signal-to-noise ratio decreases.

6. Conclusion

The H-scan analysis implemented as a set of matched filters is capable of distinguishing relatively small shifts in scatterer transfer functions, corresponding to small changes in size of the dominant scatterers within a region. The effects of frequency-dependent attenuation can be a confounding factor at increasing depths, however a zone approach to attenuation correction can be carried out to mitigate these effects, at least to some noise-limited depth. These analyses can be cast into a deterministic framework whereby many types of scatterers encountered by an incident bandpass pulse have a scattering transfer function that is modeled as a power law. The general trend is for smaller structures to have higher power laws. Within natural structures of soft tissues, the power law γ will frequently lie above 0 and below 2, with many important changes in tissue due to pathologies resulting in subtle shifts from baseline values. The clinical uses of H-scan, providing greater discrimination of subtle changes in tissue due to pathology, is potentially broad. Applications extend from cancer detection and staging to a variety of diffuse diseases such as steatosis of the liver, so long as a shift in the underlying scattering is present. This has been a goal of tissue characterization efforts for decades.

Acknowledgments

This work was support by National Institutes of Health grant R21EB025290. The authors also thank: Terri Swanson of Pfizer Inc. for the fibrosis data; Dr. Rifat Ahmed and Dr Marvin Doyley of the University of Rochester Department of Electrical and Computer Engineering for the data from the metastatic tumor model; and Dr Luis Ruffolo of the University of Rochester Medical Center Department of Surgery for data from the spontaneous murine tumor scans.

ORCID iDs

Kevin J Parker https://orcid.org/0000-0002-6313-6605

References

Abramowitz M and Stegun I A 1964 *Handbook of Mathematical Functions with Formulas, Graphs, and Mathematical Tables* (Washington: US Govt. Print. Off.)

Ahmed R, Ye J, Gerber S A and Doyely M M 2020 Preclinical imaging using single track location shear wave elastography: monitoring the progression of murine pancreatic tumor liver metastasis *in vivo IEEE Trans. Med. Imaging* Epub ahead of print

Astheimer J P and Parker K J 2018 Concentric layered Hermite scatterers *Phys. Lett.* A **382** 1379–82

Bamber J C 1979 Theoretical modelling of the acoustic scattering structure of human liver *Acoust. Lett.* **3** 114–9

Bamber J C and Dickinson R J 1980 Ultrasonic B-scanning: a computer simulation *Phys. Med. Biol.* **25** 463–79

Bilgutay N M and Saniie J 1984 The effect of grain size on flaw visibility enhancement using split-spectrum processing *Mater. Eval.* **42** 808–14

Bilgutay N M, Saniie J, Furgason E S and Newhouse V L 1979 Flaw-to-grain echo enhancement *Proceedings, Ultrasonics international* **79** 276–85

Born M and Wolf E 1980 *Principles of Optics : Electromagnetic Theory of Propagation, Interference and Diffraction of Light* (Oxford ; New York: Pergamon)

Bracewell R N 1965 *The Fourier Transform and its Applications, chapter 12* (New York: McGraw-Hill)

Campbell J A and Waag R C 1984 Measurements of calf liver ultrasonic differential and total scattering cross sections *J. Acoust. Soc. Am.* **75** 603–11

Chivers R C 1977 The scattering of ultrasound by human tissues-some theoretical models *Ultrasound Med. Biol.* **3** 1–13

Chivers R C and Hill C R 1975 A spectral approach to ultrasonic scattering from human tissue: methods, objectives and backscattering measurements *Phys. Med. Biol.* **20** 799–815

Cloostermans M J T M and Thijssen J M 1983 A beam corrected estimation of the frequency dependent attenuation of biological tissues from backscattered ultrasound *Ultrason. Imaging* **5** 136–47

Debye P and Bueche A M 1949 Scattering by an inhomogeneous solid *J. Appl. Phys.* **20** 518–25

Faran J J Jr 1951 Sound scattering by solid cylinders and spheres *J. Acoust. Soc. Am.* **23** 405–18

Fujii Y, Taniguchi N, Itoh K, Shigeta K, Wang Y, Tsao J W, Kumasaki K and Itoh T 2002 A new method for attenuation coefficient measurement in the liver: comparison with the spectral shift central frequency method *J Ultrasound Med* **21** 783–8

Galloway R L, McDermott B A and Thurstone F L 1988 A frequency diversity process for speckle reduction in real-time ultrasonic images *IEEE Trans. Ultrason. Ferroelectr. Freq. Control* **35** 45–9

Garra B S, Insana M F, Shawker T H and Russell M A 1987 Quantitative estimation of liver attenuation and echogenicity: normal state versus diffuse liver disease *Radiology* **162** 61–7

Ge G R, Laimes R, Pinto J, Guerrero J, Chavez H, Salazar C, Lavarello R J and Parker K J 2018 H-scan analysis of thyroid lesions *J Med Imaging* **5** 013505

Gore J C and Leeman S 1977 Ultrasonic backscattering from human tissue: a realistic model *Phys. Med. Biol.* **22** 317–26

Gramiak R, Hunter L P, Lee P P K, Lerner R M, Schenk E and Waag R C 1976 Diffraction characterization of tissue using ultrasound *IEEE Int. Ultrasonics Symp.* 60–3

Han B J, Ruffolo L I, Jackson K M, Belt B A, Figueroa N, Murphy J D, Linehan D and Prieto P A 2019 Investigating the tumor-immune microenvironment in an autochthonous murine model of cholangiocarcinoma *Journal of clinical oncology : official journal of the American Society of Clinical Oncology* **37** 53

Insana M F and Brown D G 1993 Acoustic scattering theory applied to soft biological tissues *Ultrasonic Scattering in Biological Tissues* ed K K Shung and G A Thieme (Boca Raton: CRC Press) pp 75–124

Insana M F, Wagner R F, Brown D G and Hall T J 1990 Describing small-scale structure in random media using pulse-echo ultrasound *J. Acoust. Soc. Am.* **87** 179–92

Javanaud C 1989 The application of a fractal model to the scattering of ultrasound in biological media *J. Acoust. Soc. Am.* **86** 493–6

Khairalseed M, Brown K, Parker K J and Hoyt K 2019a Real-time H-scan ultrasound imaging using a Verasonics research scanner *Ultrasonics* **94** 28–36
Khairalseed M, Hoyt K, Ormachea J, Terrazas A and Parker K J 2017 H-scan sensitivity to scattering size *J Med Imaging* **4** 043501
Khairalseed M, Javed K, Jashkaran G, Kim J W, Parker K J and Hoyt K 2019b Monitoring early breast cancer response to neoadjuvant therapy using H-scan ultrasound imaging: preliminary preclinical results *J Ultrasound Med* **38** 1259–68
Kuc R 1984 Estimating acoustic attenuation from reflected ultrasound signals: comparison of spectral-shift and spectral-difference approaches *IEEE Trans Acoust Speech* **32** 1–6
Lee D Y, Yoo Y, Song T K and Chang J H 2012 Adaptive dynamic quadrature demodulation with autoregressive spectral estimation in ultrasound imaging *Biomed Signal Proces* **7** 371–8
Lizzi F L, Greenebaum M, Feleppa E J, Elbaum M and Coleman D J 1983 Theoretical framework for spectrum analysis in ultrasonic tissue characterization *J. Acoust. Soc. Am.* **73** 1366–73
Macovski A 1983 *Basic Ultrasonic Imaging* (Englewood Cliffs, N.J.: Prentice-Hall)
Maklad N F, Ophir J and Balsara V 1984 Attenuation of ultrasound in normal liver and diffuse liver disease *in vivo Ultrason. Imaging* **6** 117–25
Mamou J and Oelze M L 2013 *Quantitative Ultrasound in Soft Tissues* (Dordrecht: Springer Netherlands)
Montaldo G, Tanter M, Bercoff J, Benech N and Fink M 2009 Coherent plane-wave compounding for very high frame rate ultrasonography and transient elastography *IEEE Trans. Ultrason. Ferroelectr. Freq. Control* **56** 489–506
Morse P M and Ingard K U 1987 *Theoretical Acoustics* chapter 8 (Princeton, NJ: Princeton University Press)
Nam K, Zagzebski J A and Hall T J 2013 Quantitative assessment of *in vivo* breast masses using ultrasound attenuation and backscatter *Ultrason. Imaging* **35** 146–61
Parker K J 1983 Ultrasonic attenuation and absorption in liver tissue *Ultrasound Med. Biol.* **9** 363–9
Parker K J 2016a The H-scan format for classification of ultrasound scattering *J OMICS Radiol.* **5** 1000236
Parker K J 2016b Scattering and reflection identification in H-scan images *Phys. Med. Biol.* **61** L20–8
Parker K J 2017 Hermite scatterers in an ultraviolet sky *Phys. Lett.* A **381** 3845–8
Parker K J 2019a The first order statistics of backscatter from the fractal branching vasculature *J Acoust Soc Am* **146** 3318–26
Parker K J 2019b Shapes and distributions of soft tissue scatterers *Phys. Med. Biol.* **64** 175022
Parker K J, Carroll-Nellenback J J and Wood R W 2019 The 3D spatial autocorrelation of the branching fractal vasculature *Acoustics* **1** 369–81
Parker K J, Lerner R M and Waag R C 1984 Attenuation of ultrasound: magnitude and frequency dependence for tissue characterization *Radiology* **153** 785–8
Parker K J and Tuthill T A 1986 Carbon tetrachloride induced changes in ultrasonic properties of liver *IEEE Trans. Biomed. Eng.* **33** 453–60
Parker K J, Tuthill T A and Baggs R B 1988 The role of glycogen and phosphate in ultrasonic attenuation of liver *J. Acoust. Soc. Am.* **83** 374–8
Parker K J and Waag R C 1983 Measurement of ultrasonic attenuation within regions selected from B-Scan images *IEEE Trans. Biomed. Eng.* **BME-30** 431–7
Poularikas A D 2010 *Transforms and Applications Handbook chapter 7* (Boca Raton: CRC Press)
Prince J L and Links J M 2015 *Medical Imaging Signals and Systems* (Boston: Pearson)
Rayleigh L 1918 On the scattering of light spherical shells, and by complete spheres of periodic structure, when the refractivity is small *Proceedings of the Royal Society of London. Series* A **94** 296–300
Soares K C *et al* 2014 A preclinical murine model of hepatic metastases *J. Vis. Exp.* **91** 51677
Tai H, Khairalseed M and Hoyt K 2020 Adaptive attenuation correction during H-scan ultrasound imaging using K-means clustering *Ultrasonics* **102** 105987
Waag R C, Gramiak R, Lernel R M and Schenk E A 1976 Tissue macrostructure from utlrasound scattering *Proc. Conf. on Computerised Tomography in Radiology* (St. Louis: American College of Radiology) pp 175–86
Wear K A, Garra B S and Hall T J 1995 Measurements of ultrasonic backscatter coefficients in human liver and kidney *in vivo J. Acoust. Soc. Am.* **98** 1852–7
Wei C, Chen W, Fang J and Holm S 2018 A Survey on fractional derivative modeling of power-law frequency-dependent viscous dissipative and scattering attenuation in acoustic wave propagation *Appl. Mech. Rev.* **70** 030802
Zagzebski J A, Lu Z F and Yao L X 1993 Quantitative ultrasound imaging: *in vivo* results in normal liver *Ultrason. Imaging* **15** 335–51